Sound radiation and suppression of an unbaffled long enclosure using Helmholtz resonators

Weiping Yang, Yatsze Choy[*], Zhibo Wang, Ying Li

Department of Mechanical Engineering, The Hong Kong Polytechnic University, Hung Hom, Kowloon,

Hong Kong SAR, People's Republic of China

[*] Corresponding author.
  E-mail address: mmyschoy@polyu.edu.hk (Y. S. Choy).

1

Abstract

Theoretical, numerical, and experimental investigations are presented to predict and suppress the noise radiated from monopole point sources inside an unbaffled long enclosure including the ground. First, a mathematical model is established to calculate the acoustical fields. The modal superposition method is adopted to express the sound pressure inside the long enclosure, while the radiated noise is described by applying the Wiener-Hopf (W-H) technique. Subsequently, the interior and exterior acoustical fields are coupled using the continuity equations of sound pressure and particle velocity at the opening. After that, the theoretical model is validated through the finite element method. The formation mechanisms of sound peaks, lobes, the shadow, and illuminated zones are explained from the perspective of mode theory. Meanwhile, Helmholtz resonators (HRs) are proposed to control the dominant modal responses at the opening so that the radiated noise near the resonant frequencies is attenuated. Afterwards, the relationship between acoustic modes and radiation patterns is analyzed. The HR array locations, optimized to reduce the radiated noise, are obtained. Besides, the influences of different types of noise sources on the radiated acoustic field are explored. Finally, a quasi-two-dimensional experiment is carried out to verify the proposed model and examine the feasibility of HRs in suppressing the noise radiated from an unbaffled long enclosure including the ground. This study facilitates the understanding of physics behind the sound radiation phenomenon and provides new insights into noise control strategies.

Keywords: Sound radiation; Unbaffled long enclosure; Wiener-Hopf technique; Helmholtz resonators

1. Introduction

Abatement of traffic noise using a single sound barrier or parallel barriers is common in densely populated cities. The noise level behind a barrier can be significantly reduced as the line-of-sight from the source to the receiver is intercepted, and only the diffracted sound can reach the shadow zone. To further enhance the performance, barriers with T-shaped, Y-shaped, circular, and branched edge profiles have been designed to minimize the diffracted sound waves [1]. However, their performance might not be good if the barriers were built near high-rise buildings, as the noise can still deteriorate the living conditions of high-floor residents who are exposed to the illuminated zones of these barriers [2, 3]. To effectively block the noise radiated from vehicles on the road, tunnel-shaped sound barriers or so-called soundproof tunnels have been introduced [4]. Most of the sound energy is trapped inside soundproof tunnels, as it is difficult for sound waves to penetrate the walls, which can be considered acoustically rigid. Nevertheless, inside a soundproof tunnel, which is a long and narrow space, sound waves do not dissipate but rather reverberate. Such an acoustical environment not only exerts negative psychological impacts on working staff, drivers, and passengers but also reduces the speech transmission index [5, 6]. Moreover, as sound waves can only escape from the exits at the ends of soundproof tunnels, the sound radiated from the portals becomes the dominant source of noise pollution to the surroundings. Therefore, it is necessary to explore the formation mechanisms of sound fields inside and outside a soundproof tunnel so that appropriate noise attenuation approaches can be proposed.

The geometrical configurations of a soundproof tunnel can be represented by an unbaffled long enclosure including the ground, as demonstrated in Refs. [5-8]. The generation and propagation of sound waves inside long enclosures or soundproof tunnels have been well investigated in recent years. The image source method (ISM) [8] and the classical wave theory [9] are frequently utilized.

3

Little effort, however, has been devoted to the establishment of a prediction model for sound radiation from an unbaffled long enclosure, especially when the ground is taken into consideration. For such a complex geometry, numerical approaches, including the finite element method (FEM) [10, 11] and boundary element method (BEM) [12, 13], can be adopted. However, their calculation efficiency declines rapidly due to the substantial increase in the number of meshing elements when calculating large acoustical domains. Apart from numerical methods, the Research Committee on Road Traffic Noise of the Acoustical Society of Japan (ASJ) published the ASJ model to calculate the noise radiated from a traffic tunnel [14]. The diffraction at the tunnel edge and the reflection of the ground are included by adding extra correction terms to the sound propagation equation. These terms, however, are not obtained through theoretical derivations but fitted from scaled-down experimental data. As a result, the ASJ model may give rise to inaccurate predictions when it is applied to engineering projects. In addition to the aforementioned models, the Wiener-Hopf (W-H) technique has been adopted to calculate the sound pressure level (SPL) radiated from annular pipes [15]. Recently, the sound radiation from an unbaffled long enclosure with the ground was formulated by applying the W-H technique [7]. The diffraction at the enclosure edge and the reflection on the ground were rigorously considered in that model. Moreover, the far-field directivity pattern of the radiated sound field was expressed explicitly in terms of the observation radius and angle, which can be applied to calculate large acoustical domains with high efficiency. Therefore, we adopt the W-H technique in the current study to model sound radiation from a soundproof tunnel and explore the physics behind the sound radiation phenomenon.

To effectively reduce the noise radiated from the portals of a soundproof tunnel using a confined space, a simple, reliable, and compact noise control device is needed. Recently, Wang et al. [16-18] proposed an active noise control (ANC) system called the planar virtual sound barrier to attenuate

the sound radiated from a baffled rectangular cavity. Although substantial noise reductions were achieved near the resonant frequencies of the cavity using the ANC system, this method can hardly be applied in practical tunnels owing to the robust and complicated requirements of the ANC system. On the other hand, passive noise attenuation techniques such as covering the inner surfaces of parallel barriers [19] and ducts [20] with porous materials have been proposed to reduce the sound radiated from openings. However, the performance is undesirable at low frequencies, and the porous materials may cause hygiene problems such as the accumulation of dust and bacteria. Recently, the concept of sound wave-trapping barriers was introduced [21], where the inner walls of the barriers are coated by wedge-shaped structures. The sound waves are either redirected towards the ground or trapped within the parallel barriers so that the noise radiated to the outside is reduced. To suppress the sound radiated from parallel barriers, Wang et al. [22, 23] adopted Helmholtz resonators (HRs) to modify the sound pressure distribution inside the parallel barriers so that the diffracted and radiated sound around the targeted frequencies were reduced with an appropriate number and appropriate positions of HRs. The performance of HRs, however, is still limited by relatively narrow working frequency bands. To widen the stopband, a flexible panel device (FPD) was proposed to be mounted on the walls of the parallel barriers [24]. An average insertion loss (IL) of approximately 5 dB was achieved in the frequency range of 80 Hz and 1000 Hz. Moreover, with the advancement of acoustic meta-surfaces, parallel barriers of inhomogeneous impedance were constructed using an array of slender tubes with varying depths [25-27]. The reflected waves were manipulated by the phase gradient of the walls so that the trapped acoustical energy inside the barrier was altered, which improved the sound reduction in the shadow zone.

In the current study, the sound field inside an unbaffled long enclosure is expressed in terms of the superposition of acoustic modes, and the radiated sound field is related to the modal expansions

of pressure and particle velocity at the opening. To distort the acoustic modal responses inside the long enclosure, mounting HRs on the wall is proposed. The modal responses at the opening around the targeted frequencies are reduced, and the radiated noise is expected to be suppressed. Although HRs have been widely adopted to attenuate the noise in open cavities [22, 23], ducts [28, 29], and enclosure systems [30-33], the interaction between HRs and the acoustic field inside an unbaffled long enclosure has seldom been investigated.

In this study, we focus on the formation and suppression mechanisms of sound peaks and directivity patterns of the radiated acoustic field from the perspective of mode theory. Additionally, different types of sound sources are considered to mimic practical scenarios. Moreover, to validate the theoretical model and examine the performance of HRs in reducing the radiated noise, a quasi-two-dimensional experiment is implemented. In summary, the objectives of this study are (1) to establish a theoretical model for the prediction of sound fields inside and outside an unbaffled long enclosure including the ground based on the W-H technique and the mode-matching method; (2) to investigate the formation and suppression mechanisms of sound peaks and directivity patterns from the perspective of mode theory; (3) to explore the performance of HRs in controlling the radiated noise from a long enclosure, especially in the shadow zone; and (4) to validate the theoretical model and confirm the feasibility of HRs in reducing the radiated noise from long enclosures via a quasi-two-dimensional experiment. The remainder of this paper is organized as follows. The theoretical model is first formulated in Section 2. Modal analysis and mechanism investigations are then carried out in Section 3. Experimental results are provided in Section 4, and conclusions are finally drawn in Section 5.

2. Formulation

2.1. Description of the problem in the natural domain

A schematic diagram of sound radiation from a two-dimensional (2D) unbaffled long enclosure including the ground is presented in Fig. 1. The height of the long enclosure is h, and the thickness of the wall is assumed to be zero. All the boundaries are set to be acoustically rigid for simplicity. The noise is produced by monopole point sources denoted by $S_1 \dots S_n$, where $n = 1, 2, 3 \dots$, inside the long enclosure with their locations and the volume velocity strengths being x_n, y_n, and Q_n, respectively. A Cartesian coordinate system is adopted, and the origin is fixed at the intersection of the opening and the ground. In addition, a polar coordinate system with the observation radius and angle being r and θ is also shown to express the directivity patterns of the radiated sound field. In addition, imaginary interfaces I and II are depicted for the convenience of analysis. They divide the whole acoustical domain into three subregions which are denoted by Ω_A, Ω_B, and Ω_C, respectively.
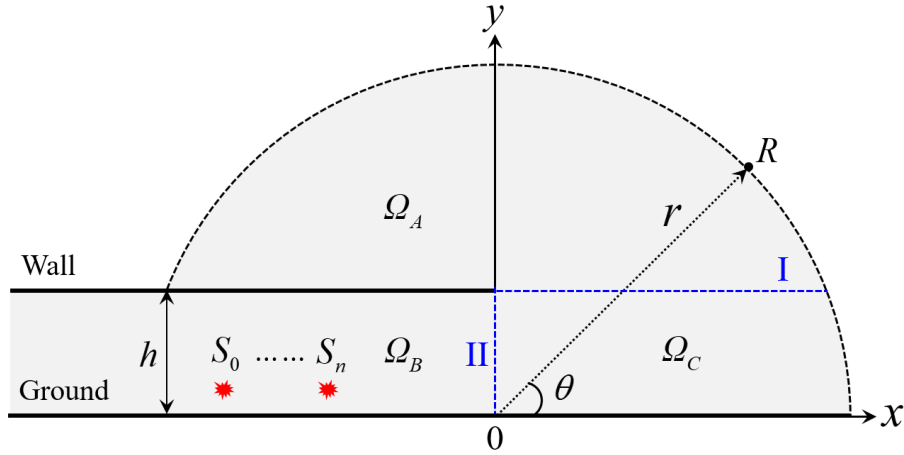

Fig. 1. Schematic diagram of sound radiation from a two-dimensional unbaffled long enclosure including the ground.

According to the partition of the whole acoustical domain presented in Fig. 1, the total sound pressure field is expressed by the following piecewise function as

$$p_{total}(x,y) = \begin{cases} p_A(x,y), & \Omega_A : x \in (-\infty, +\infty), y \in [h, +\infty) \\ p_{incident}(x,y) + p_{reflected}(x,y), & \Omega_B : x \in (-\infty, 0], y \in [0, h], \\ p_C(x,y), & \Omega_C : x \in [0, +\infty), y \in [0, h] \end{cases} \tag{1}$$

where $p_A(x,y)$ and $p_C(x,y)$ are the sound pressure fields in regions Ω_A and Ω_C, respectively. The incident and reflected sound pressure fields of region Ω_B are denoted by $p_{incident}(x,y)$ and $p_{reflected}(x,y)$, respectively. The total sound pressure field without any source satisfies the homogeneous Helmholtz equation as

$$\left(\nabla^2 + k^2 \right) p_{total}(x,y) = 0, \tag{2}$$

where $\nabla^2 = \partial^2/\partial x^2 + \partial^2/\partial y^2$ denotes the 2D Laplace operator, and k represents the wavenumbers in the free space. To solve the governing Eq. (2), rigid boundary conditions on the ground and wall surfaces are considered as follows:

$$\frac{\partial p_{total}(x,y)}{\partial y} = 0 \left| \begin{array}{l} y = h^\pm, \quad x \in (-\infty, 0] \\ y = 0^+, x \in (-\infty, +\infty) \end{array} \right. . \tag{3}$$

In addition, continuity equations of sound pressure and particle velocity at imaginary interfaces I and II are expressed as follows to couple the acoustical fields:

$$p_A = p_C, \frac{\partial p_A}{\partial y} = \frac{\partial p_C}{\partial y} \bigg|_I ; \; p_B = p_C, \frac{\partial p_B}{\partial x} = \frac{\partial p_C}{\partial x} \bigg|_{II} \tag{4}$$

where p_B denotes the sound pressure field of region Ω_B.

Besides, the Sommerfeld radiation condition is considered to describe the propagation of sound waves in the semi-infinite region outside the long enclosure [21]:

$$\lim_{r \to \infty} \sqrt{r}\left[\frac{\partial p_{total}(r,\theta)}{\partial r} - ikp_{total}(r,\theta)\right] = 0, \quad r = \sqrt{x^2 + y^2} , \tag{5}$$

Also, to avoid the geometrical singularity at the enclosure edge, and ensure the uniqueness of the solution, the acoustical energy stored in any finite neighborhood of the edge must be finite [34]:

$$p_{total}(x,h) = O\left(|x|^{1/2}\right), \quad \frac{\partial p_{total}(x,h)}{\partial y} = O\left(|x|^{-1/2}\right), \quad |x| \to 0 , \tag{6}$$

where O is infinitesimal of higher-order. Inside the long enclosure, the incident sound pressure produced by the *n-th* monopole point source satisfies the following inhomogeneous Helmholtz equation:

$$\left(\nabla^2 + k^2\right) p_{incident}(x,y) = -i\rho kc_0 Q_n \delta(x-x_n)(y-y_n) , \tag{7}$$

where δ, ρ, and c_0 denote the Dirac delta function, air density, and sound speed, respectively. Based on the boundary condition Eq. (3) and the superposition principle of sound pressure, the total incident sound pressure field produced by multiple point sources is expressed as

$$p_{incident}(x,y) = \sum_{n=1}^{\infty}\sum_{j=0}^{\infty} \frac{\rho kc_0 Q_n \cos(\kappa_j y_n)\cos(\kappa_j y)}{2\Lambda_j \alpha_j} e^{-i\alpha_j|x-x_n|} , \tag{8}$$

where the transversal and horizontal wavenumbers inside the long enclosure, the normalized coefficients of the modal expansion are calculated by

$$\kappa_j = \frac{j\pi}{h}, \quad \alpha_j = \sqrt{k^2 - \kappa_j^2}, \quad \Lambda_j = \frac{h}{2}(1+\delta_{oj}), \quad j = 0,1,2,.... . \tag{9}$$

Due to the impedance mismatch caused by the abrupt size change at two sides of the enclosure opening, there is a reflected sound pressure field inside the long enclosure:

$$p_{reflected}(x,y) = \sum_{j=0}^{\infty} b_j \cos(\kappa_j y) e^{i\alpha_j x} , \tag{10}$$

where b_j stands for the modal response coefficient.

To date, the boundary value problem has been described in the natural domain. However, due to the infinite boundary conditions outside the long enclosure, it is difficult to obtain a solution to the Helmholtz equation by applying traditional methods. Inspired by the corresponding relationship between the infinite boundary conditions and the infinite limits of the Fourier integral, next, we apply the Fourier transform to convert the radiated sound pressure field into the spectral domain. A solvable W-H equation is obtained and then solved through the W-H technique.

2.2. Radiated sound pressure field in the spectral domain

The Helmholtz equation for region Ω_A in the natural domain can be converted into the spectral domain via the full-range Fourier transform in terms of x as

$$\int_{-\infty}^{+\infty}\left[\frac{\partial^2 p_A(x,y)}{\partial x^2}+\frac{\partial^2 p_A(x,y)}{\partial y^2}+k^2 p_A(x,y)\right]e^{-i\alpha x}dx=0, \tag{11}$$

where $i=\sqrt{-1}$ and α denotes the Fourier transform variable. The first term in the bracket of Eq. (11) can be integrated by parts as

$$\int_{-\infty}^{+\infty}\frac{\partial^2 p_A(x,y)}{\partial x^2}e^{-i\alpha x}dx=\left[\frac{\partial p_A(x,y)}{\partial x}e^{-i\alpha x}\right]_{-\infty}^{+\infty}$$
$$+i\alpha\left[p_A(x,y)e^{-i\alpha x}\right]_{-\infty}^{+\infty}-\alpha^2\int_{-\infty}^{+\infty}p_A(x,y)e^{-i\alpha x}dx=-\alpha^2 P_A(\alpha,y) \tag{12}$$

where

$$P_A(\alpha,y)=\int_{-\infty}^{+\infty}p_A(x,y)e^{-i\alpha x}dx \tag{13}$$

represents the transformed sound pressure field of region Ω_A in the complex α-plane. Hereafter, we use the upper-case of the natural domain variables to represent their transformed forms in the spectral domain. Note that the contributions from the bracketed terms of Eq. (12) at positive and negative infinity are both

10

zero. They result from the Sommerfeld radiation condition, which states that outgoing waves disappear at infinity. Finally, the transformed Helmholtz equation for region Ω_A is expressed as

$$\left[\frac{\partial^2}{\partial y^2}+\kappa^2(\alpha)\right]P_A(\alpha,y)=0,\tag{14}$$

where $\kappa(\alpha)=\sqrt{k^2-\alpha^2}$, which is called the square root function, is defined in the complex α-plane. For later convenience, we define the upper and lower halves of the complex α-plane. A schematic diagram of the branch points, branch cuts, and complex half-planes can be found in Ref. [7]. The transformed sound pressure field of region Ω_A can be divided into positive and negative parts according to the definition of the half-range Fourier transform as

$$P_A(\alpha,y)=P_A^-(\alpha,y)+P_A^+(\alpha,y)=\int_{-\infty}^{0}p_A(x,y)e^{-i\alpha x}dx+\int_{0}^{+\infty}p_A(x,y)e^{-i\alpha x}dx.\tag{15}$$

Based on the following asymptotic behavior:

$$p_A(x,y)=O\left(e^{-ik|x|}\right),\quad x\to\pm\infty,\tag{16}$$

it can be observed that $P_A^+(\alpha,y)$ and $P_A^-(\alpha,y)$ are regular functions in the upper and lower halves of the complex α-plane, respectively. The solution to Eq. (14) satisfying the Sommerfeld radiation condition is expressed as

$$P_A(\alpha,y)=A(\alpha)e^{-i\kappa(\alpha)(y-h)},\tag{17}$$

where $A(\alpha)$ represents an unknown spectral coefficient. Combining Eqs. (15), (17), and the transformed boundary condition on the outside wall: $\dot{P}_A^-(\alpha,h)=0$, where the dot represents the derivative to y, we have the following identity:

$$\dot{P}_A^+(\alpha,h)=-i\kappa(\alpha)A(\alpha),\tag{18}$$

where $\dot{P}_A^+(\alpha,h)$ denotes an important intermediate term. Once it is determined, the transformed sound pressure field of region Ω_A can be obtained by Eqs. (17) and (18). Then, through the inverse Fourier transform of Eq. (17), the sound pressure field of region Ω_A in the natural domain can be attained.

Similarly, the transformed Helmholtz equation for region Ω_C in the spectral domain can be obtained using the half-range Fourier transform with respect to x as

$$\left[\frac{\partial^2}{\partial y^2}+\kappa^2(\alpha)\right]P_C^+(\alpha,y)=f(y)+i\alpha g(y), \tag{19}$$

where the following definitions are used to denote the sound pressure and its gradient at the opening:

$$g(y)=p_C(0,y), \ f(y)=\frac{\partial p_C(0,y)}{\partial x}, \tag{20}$$

and

$$P_C^+(\alpha,y)=\int_0^{+\infty}p_C(x,y)e^{-i\alpha x}dx. \tag{21}$$

The general solution to Eq. (19), which is a second-order inhomogeneous linear differential equation, is obtained using the method of constant variation as

$$
\begin{aligned}
P_C^+(\alpha,y)&=B(\alpha)\cos\left[\kappa(\alpha)y\right]+C(\alpha)\sin\left[\kappa(\alpha)y\right]\\
&+\frac{1}{\kappa(\alpha)}\int_0^y\left[f(\varsigma)+i\alpha g(\varsigma)\right]\sin\left[\kappa(\alpha)(y-\varsigma)\right]d\varsigma
\end{aligned}, \tag{22}
$$

where $B(\alpha)$ and $C(\alpha)$ are unknown spectral coefficients, and ς is an integration variable. Using the transformed continuity equation of particle velocity at imaginary interface I: $\dot{P}_A^+(\alpha,h)=\dot{P}_C^+(\alpha,h)$, the sound pressure field of region Ω_C in the spectral domain is obtained:

$$P_C^+(\alpha, y) = -\frac{\cos[\kappa(\alpha)y]}{\kappa(\alpha)\sin[\kappa(\alpha)h]}$$

$$\times \left\{ \dot{P}_A^+(\alpha,h) - \int_0^h [f(\varsigma) + i\alpha g(\varsigma)]\cos[\kappa(\alpha)(h-\varsigma)]d\varsigma \right\}. \tag{23}$$

$$+ \frac{1}{\kappa(\alpha)}\int_0^y [f(\varsigma) + i\alpha g(\varsigma)]\sin[\kappa(\alpha)(y-\varsigma)]d\varsigma$$

The left-hand side (LHS) term of Eq. (23) is regular in the upper half complex α-plane. However, the regularity of the right-hand side (RHS) terms is violated by the presence of poles occurring at the zeros of the denominator, which gives

$$\kappa(\alpha_m) = \kappa_m = \frac{m\pi}{h}, \quad \alpha_m = \sqrt{k^2 - \kappa_m^2}, \quad m = 0,1,2,.... \tag{24}$$

These first-order poles can be eliminated by imposing that their residues are zero. According to the residue theorem, the terms in the bracket of Eq. (23) should be zero which gives

$$\dot{P}_A^+(\alpha_m,h) = (-1)^m \int_0^h [f(\varsigma) + i\alpha_m g(\varsigma)]\cos[\kappa(\alpha_m)\varsigma]d\varsigma. \tag{25}$$

According to the form of the terms in the integrand of Eq. (25), we define two coefficients as

$$\begin{bmatrix} g_m \\ f_m \end{bmatrix} = \frac{1}{\Lambda_m^C}\int_0^h \begin{bmatrix} g(\varsigma) \\ f(\varsigma) \end{bmatrix}\cos(\kappa_m\varsigma)d\varsigma, \tag{26}$$

where the normalized coefficient of these series expansions is expressed as

$$\Lambda_m^C = \frac{h}{2}(1 + \delta_{om}), \tag{27}$$

Substituting Eq. (26) into Eq. (25), the residue solution is expressed as

$$\dot{P}_A^+(\alpha_m,h) = \Lambda_m^C (f_m + i\alpha_m g_m)(-1)^m. \tag{28}$$

As can be seen in Eq. (28), there are still two unknowns f_m and g_m to be solved. Next, we continue to find extra equations to determine them.

13

2.3. W-H equation and its solution

In this section, a W-H equation in the complex α-plane is obtained using the continuity equation at the imaginary interface I. Considering Eqs. (15), (17), (18), and the transformed form of the sound pressure continuity equation at the imaginary interface I, namely, $P_A^+(\alpha,h) = P_C^+(\alpha,h)$, the following identity is attained:

$$P_C^+(\alpha,h) + P_A^-(\alpha,h) = \frac{i}{\kappa(\alpha)} \dot{P}_A^+(\alpha,h).$$
(29)

Substituting Eq. (23) into Eq. (29), we have

$$\frac{\dot{P}_A^+(\alpha,h)}{\kappa^2(\alpha)L(\alpha)} - P_A^-(\alpha,h)$$

$$= \frac{1}{\kappa(\alpha)\sin[\kappa(\alpha)h]} \int_0^h [f(\varsigma) + i\alpha g(\varsigma)]\cos[\kappa(\alpha)\varsigma]d\varsigma$$
(30)

where the kernel function is defined as

$$L(\alpha) = \frac{\sin[\kappa(\alpha)h]}{\kappa(\alpha)} e^{-i\kappa(\alpha)h}.$$
(31)

Based on Eq. (26), we can express the defined functions in the form of series expansions as

$$\begin{bmatrix} g(y) \\ f(y) \end{bmatrix} = \sum_{m=0}^{\infty} \begin{bmatrix} g_m \\ f_m \end{bmatrix} \cos(\kappa_m y).$$
(32)

Evaluating the obtained integration in Eq. (30), we obtain the following W-H equation of the second kind, which is valid in the overlapped region of the upper and lower halves of the complex α-plane:

$$\frac{\dot{P}_A^+(\alpha,h)}{\kappa^2(\alpha)L(\alpha)} - P_A^-(\alpha,h) = -\sum_{m=0}^{\infty}(f_m + i\alpha g_m)\frac{(-1)^m}{\alpha^2 - \alpha_m^2}.$$
(33)

The formal solution of Eq. (33) can be obtained through the classical W-H procedures. The first step is to split the kernel functions into positive and negative functions, which are analytic in the upper and lower halves of the complex α-plane, respectively. The factorization result is given by

$$
\frac{\dot{P}_A^+(\alpha,h)}{\kappa^+(\alpha)\kappa^-(\alpha)L^+(\alpha)L^-(\alpha)} - P_A^-(\alpha,h)
$$
$$
= -\sum_{m=0}^{\infty}(-1)^m\left[\frac{f_m+i\alpha_m g_m}{2\alpha_m(\alpha-\alpha_m)} - \frac{f_m-i\alpha_m g_m}{2\alpha_m(\alpha+\alpha_m)}\right], \tag{34}
$$

where $L^+(\alpha)$ and $\kappa^+(\alpha)$ denote regular split functions in the upper half of the complex α-plane. The explicit expressions of these functions are obtained based on the method described by Mitta [35] as

$$
L^+(\alpha) = \sqrt{\frac{\sin(kh)}{k}} \times \exp\left\{\ln\left[\frac{\alpha-i\kappa(\alpha)}{k}\right]\frac{\kappa(\alpha)h}{\pi}\right\}
$$
$$
\times\exp\left\{\left(1-C+\ln\left(\frac{2\pi}{kh}\right)-\frac{i\pi}{2}\right)\frac{-i\alpha h}{\pi}\right\}\times\prod_{m=1}^{\infty}\left(1+\frac{\alpha}{\alpha_m}\right)\times\exp\left(\frac{-i\alpha h}{m\pi}\right), \tag{35}
$$
$$
\kappa^+(\alpha) = k+\alpha
$$

where C is Euler's constant given by $C=0.57721\ldots$, and the split functions satisfy the relations below:

$$
L(\alpha) = L^+(\alpha)L^-(\alpha),\ L^+(\alpha) = L^-(-\alpha),\ \kappa(\alpha) = \kappa^+(\alpha)\kappa^-(\alpha),\ \kappa^+(\alpha) = \kappa^-(-\alpha). \tag{36}
$$

Collecting the terms that are regular in the upper half complex α-plane at the LHS, and those regular in the lower half complex α-plane at the RHS, we have

$$
\frac{\dot{P}_A^+(\alpha,h)}{\kappa^+(\alpha)L^+(\alpha)} - \sum_{m=0}^{\infty}(-1)^m\frac{f_m-i\alpha_m g_m}{2\alpha_m(\alpha+\alpha_m)}\kappa^-(\alpha)L^-(\alpha)
$$
$$
= -\sum_{m=0}^{\infty}(-1)^m\frac{f_m+i\alpha_m g_m}{2\alpha_m(\alpha-\alpha_m)}\kappa^-(\alpha)L^-(\alpha) + P_A^-(\alpha,h)\kappa^-(\alpha)L^-(\alpha). \tag{37}
$$

The regularity of the LHS terms in the lower half complex α-plane is violated by simple poles occurring at the zeros of the denominator. These poles can be eliminated using the decomposition procedure:

$$\frac{\dot{P}_A^+(\alpha,h)}{\kappa^+(\alpha)L^+(\alpha)} - \sum_{m=0}^{\infty}(-1)^m \frac{f_m - i\alpha_m g_m}{2\alpha_m(\alpha+\alpha_m)}\left[\kappa^-(\alpha)L^-(\alpha) - \kappa^-(-\alpha_m)L^-(-\alpha_m)\right]$$

$$-\sum_{m=0}^{\infty}(-1)^m \frac{f_m - i\alpha_m g_m}{2\alpha_m(\alpha+\alpha_m)}\kappa^-(-\alpha_m)L^-(-\alpha_m) \qquad . \qquad (38)$$

$$= -\sum_{m=0}^{\infty}(-1)^m \frac{f_m + i\alpha_m g_m}{2\alpha_m(\alpha-\alpha_m)}\kappa^-(\alpha)L^-(\alpha) + P_A^-(\alpha,h)\kappa^-(\alpha)L^-(\alpha)$$

Considering the analytical continuation followed by Liouville's theorem and making full use of the properties of the split functions in Eq. (36), the W-H solution is obtained as

$$\dot{P}_A^+(\alpha,h) = \sum_{m=0}^{\infty}(-1)^m \frac{f_m - i\alpha_m g_m}{2\alpha_m(\alpha+\alpha_m)}\kappa^+(\alpha_m)\kappa^+(\alpha)L^+(\alpha_m)L^+(\alpha). \qquad (39)$$

2.4. Sound pressure fields in the natural domain

To determine the unknown modal response coefficients in Eqs. (28) and (39), we now employ the well-known mode-matching method, which has been extensively applied to analyze the sound fields inside waveguide structures. Using the continuity equations for sound pressure and particle velocity at the opening, we have

$$\sum_{m=0}^{\infty} g_m \cos(\kappa_m y) = \sum_{n=1}^{\infty}\sum_{j=0}^{\infty} \frac{\rho k c_0 Q_n \cos(\kappa_j y_n)\cos(\kappa_j y)}{2\Lambda_j \alpha_j}e^{i\alpha_j x_n} + \sum_{j=0}^{\infty} b_j \cos(\kappa_j y) \qquad (40)$$

$$\sum_{m=0}^{\infty} f_m \cos(\kappa_m y) = -\sum_{n=1}^{\infty}\sum_{j=0}^{\infty} \frac{i\rho k c_0 Q_n \cos(\kappa_j y_n)\cos(\kappa_j y)}{2\Lambda_j}e^{i\alpha_j x_n} + \sum_{j=0}^{\infty} i\alpha_j b_j \cos(\kappa_j y) \qquad (41)$$

Multiply both sides of Eqs. (40) and (41) by $\cos(\kappa_s y)$ and conduct an integration along the opening in terms of y. Making full use of the orthogonality of the cosine function, we have

$$g_s = \underbrace{\sum_{n=1}^{\infty} \frac{\rho k c_0 Q_n \cos(\kappa_s y_n)e^{i\alpha_s x_n}}{2\Lambda_s \alpha_s} + b_s}_{Y_{s1}} \qquad (42)$$

$$f_s = -\underbrace{\sum_{n=1}^{\infty} \frac{i\rho k c_0 Q_n \cos\left(\kappa_s y_n\right) e^{i\alpha_s x_n}}{2\Lambda_s}}_{M_{s1}} + \underbrace{i\alpha_s}_{U_{ss}} b_s \tag{43}$$

In addition, the W-H solution Eq. (28) and the residue solution Eq. (39) are equal at specific α_s. Then we have the following identity:

$$\underbrace{f_s + i\alpha_s}_{U_{ss}} g_s = \sum_{m=0}^{\infty} (-1)^m \underbrace{\frac{\kappa^+\left(\alpha_m\right) L^+\left(\alpha_m\right)\kappa^+\left(\alpha_s\right) L^+\left(\alpha_s\right)}{2\alpha_m\left(\alpha_s+\alpha_m\right)\Lambda_s\left(-1\right)^s}}_{H_{sm}} \left(f_m - \underbrace{i\alpha_m}_{U_{mm}} g_m \right) \tag{44}$$

Rewriting Eqs. (42)-(44) in matrix forms, we have

$$\mathbf{G=Y+B} \tag{45}$$

$$\mathbf{F=M+UB} \tag{46}$$

$$\mathbf{F+UG=H\left(F-UG\right)} \tag{47}$$

where $\mathbf{B}$, $\mathbf{F}$, and $\mathbf{G}$ are unknown coefficients to be determined; $\mathbf{Y}$, $\mathbf{M}$, $\mathbf{U}$, and $\mathbf{H}$ are known matrices that can be constructed according to Eqs. (42)-(44). Matrix inversions are needed in the process of solving the equations. Therefore, we let all the subscript indices be equal to guarantee that they are square matrices. After determining the unknowns, the radiated sound pressure field of region $\varOmega_A$ in the natural domain is obtained by taking the inverse Fourier transform of Eq. (17) as

$$p_A\left(x,y\right) = \frac{1}{2\pi}\int_{\Gamma} \frac{\dot{P}_A^+\left(\alpha,h\right)}{-i\kappa\left(\alpha\right)} e^{-i\kappa\left(\alpha\right)\left(y-h\right)+i\alpha x} d\alpha. \tag{48}$$

Here, the integration path Γ is a straight line along the real axis lying in the common strip of the upper and lower halves of the complex α-plane. Eq. (48) can be numerically evaluated applying the method introduced in Ref. [15]. However, direct calculation of the inverse Fourier transform is expensive and

time-consuming for large acoustical domains. To perform an asymptotic evaluation of Eq. (48), we conduct a change of variable:

$$\alpha = -k \cos w, \quad x = r \cos \theta, \quad y = r \sin \theta . \tag{49}$$

According to the procedures described in Ref. [35], the far-field directivity pattern of the radiated sound field can be approximately obtained by the saddle point method as

$$p_A(r,\theta) = i \frac{e^{i\pi/4}}{\sqrt{2\pi}} \dot{P}_A^+ \left(-k \cos \theta, h\right) e^{ik \sin \theta h} \frac{e^{-ikr}}{\sqrt{kr}} . \tag{50}$$

In the following calculations, this far-field result is applied, which is sufficient for most engineering applications. For detailed analysis, near-field solutions are needed which can be obtained by evaluating Eq. (48). Alternatively, FEM-based hybrid methods introduced in Refs. [22-24, 36] can be used to attain the near-field results.

3. Results and discussions

In this section, numerical calculations and FEM simulations are conducted to validate the theoretical model and reveal the mechanisms behind the radiation phenomenon. The height and truncated length of the long enclosure are 1 m and 5 m, respectively. We start with a single monopole point source with its volume velocity strength and location coordinates being $Q_1 = 0.01$ m²/s and (-2, 0.5) m, respectively. The density of air and the speed of sound are 1.225 kg/m³ and 340 m/s, respectively. In addition, the far-field observation radius is taken as 5 m, and the targeted frequency range is [200, 1500] Hz.

3.1. Model validation through the FEM

Before calculating any result using the theoretical model, the wavenumbers and truncated modal numbers should be determined first, as elaborated in Ref. [7]. The FEM-based commercial software COMSOL Multiphysics is applied to conduct the simulations. The directivity patterns of the radiated

SPL outside the long enclosure at different frequencies obtained by the W-H technique and the FEM are presented in a polar coordinate system, as shown in Fig. 2. Roughly speaking, the results have good agreement with each other even though there are discrepancies at specific observation angles in front of the opening that are caused by the far-field approximation. The distribution patterns of the radiated sound field can be briefly explained from the perspective of acoustical rays using Fig. 3. In the shadow zone, as shown in Fig. 3 (a), the sound field is only composed of diffracted rays that depend on the acoustic properties near the edge. The distribution of SPL in this region appears to be quite uniform. In the illuminated zone, however, the SPL distribution is complex, as presented in Fig. 3 (b), which is formed by direct sound propagation, sound reflection from the ground and wall, and sound diffraction at the edge. These sound waves propagate to the receiver with different phases and over different distances. Consequently, their superposition leads to directivity lobes in front of the enclosure opening, as presented in Fig. 2.
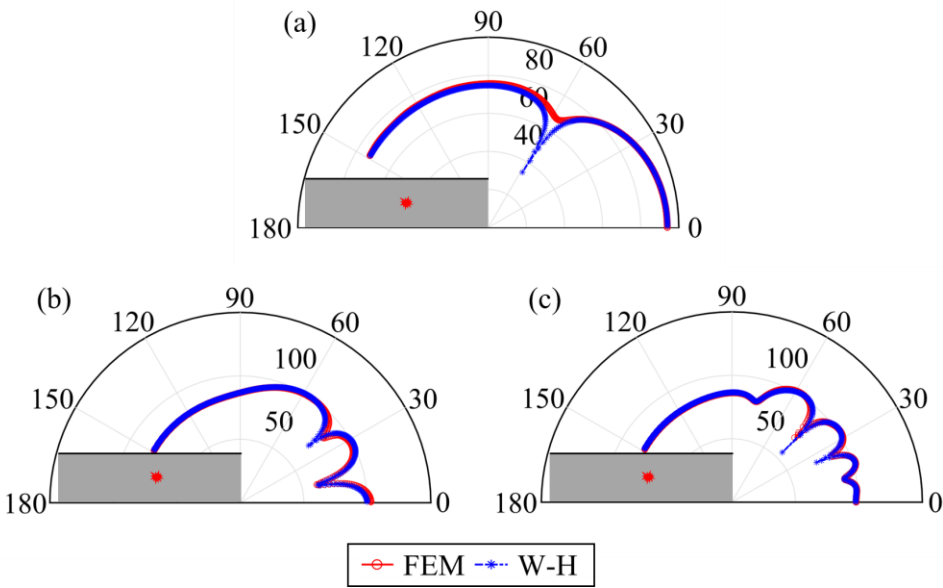
Fig. 2. Directivity patterns of the radiated SPL (dB) field obtained by the FEM and the W-H technique at (a) 200 Hz, (b) 800 Hz, and (c) 1200 Hz.
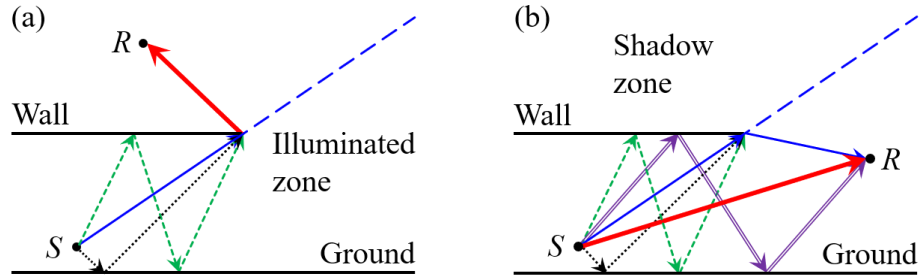
Fig. 3. Acoustical rays from the source to the receiver in (a) shadow zone, and (b) illuminated zone.

As the directivity polar plots can only show the patterns of the radiated sound field at specific frequencies, SPL spectra of two randomly picked receiving points R1 (-1, 0.5) m and R2 (-3, 3) m are used to represent the characteristics of sound fields inside and in the shadow zone of the long enclosure. The comparison between the SPLs obtained by the W-H technique and the FEM in the targeted frequency range at the receivers is illustrated in Fig. 4. Good agreement can be observed between the results, which along with Fig. 2, verifies the proposed model in the calculation of sound fields inside and outside the unbaffled long enclosure.
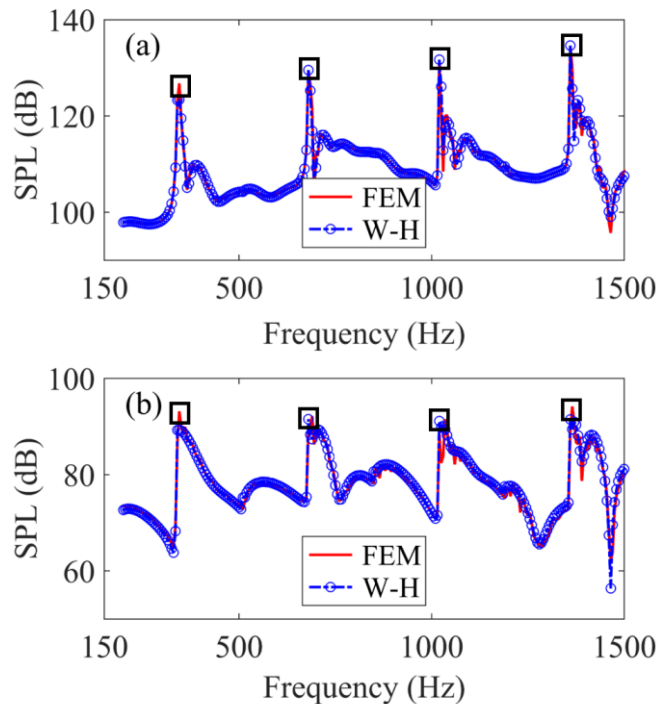
Fig. 4. Comparison of SPL spectra of receivers inside and outside the long enclosure at (a) R1 (-1, 0.5) m and (b) R2 (-3, 3) m.

3.2. Formation mechanisms of the sound fields

As demonstrated in Fig. 4, SPL peaks can be observed at approximately 340 Hz, 680 Hz, 1020 Hz, and 1360 Hz (denoted by squares), which are the resonant frequencies of the long enclosure along the vertical direction. To explore the formation mechanisms of sound peaks and then suppress the radiated noise at peak frequencies, HRs are proposed to reduce the relevant modal responses inside the long enclosure so that the radiated SPL fields around the peak frequencies are expected to be attenuated. Generally, the acoustical coupling between a long enclosure and an HR is strong when the resonator is close to the anti-node regions or near the primary sound sources [22]. In addition, the acoustical properties at the enclosure edge, according to the geometrical theory of diffraction (GTD) [37], have a great influence on the diffracted sound field. Hence, we choose two HR locations L1 (-2, 1) m and L2 (0, 1) m to explore their influences on the sound radiation phenomenon. Fig. 5 (a), (b), and (c) show the SPL distributions inside and outside a long enclosure at 340 Hz for rigid wall without and with HRs at locations L1 (denoted by HR340, L1) and L2 (denoted by HR340, L2), respectively. In Fig. 5 (a), due to multiple reflections on the rigid ground and wall, an acoustic mode can be observed, and the SPL is generally high inside the unbaffled long enclosure. However, in the horizontal direction, standing waves can hardly be seen because the reflected sound is relatively small, which only influences the sound distribution near the opening. Outside the long enclosure, the principal lobe (the lobe with the highest SPL near the enclosure edge) is located at about 70 degrees. Fig. 5 (b) shows that when the resonator is located exactly above the sound source, the SPL distribution inside the long enclosure is greatly changed, and the sound energy radiates mainly towards 10 degrees. Besides, the amplitude of the principal lobe is greatly reduced, and its angle shifts to a lower degree compared with the rigid case. In Fig. 5 (c), an HR340 is mounted at the edge, and

21

the SPL distribution inside the long enclosure remains almost the same as that in the case of rigid wall without a resonator. However, the amplitude of the principal lobe is reduced, and its angle shifts to a lower degree as well. Fig. 5 (d) illustrates the comparison of directivity patterns outside the long enclosure. The SPL distribution patterns along the observation radius are quite similar to the near-field results. However, the amplitudes and sizes of lobes are different among the three situations. In general, the sound is significantly reduced beyond the observation angle of 50 degrees when an HR340 is mounted on the enclosure wall. However, the SPLs below the observation angle of 50 degrees are mostly larger than those in the rigid case. This implies that more sound energy radiates to the lower observation angles when an HR340 is mounted on the wall.
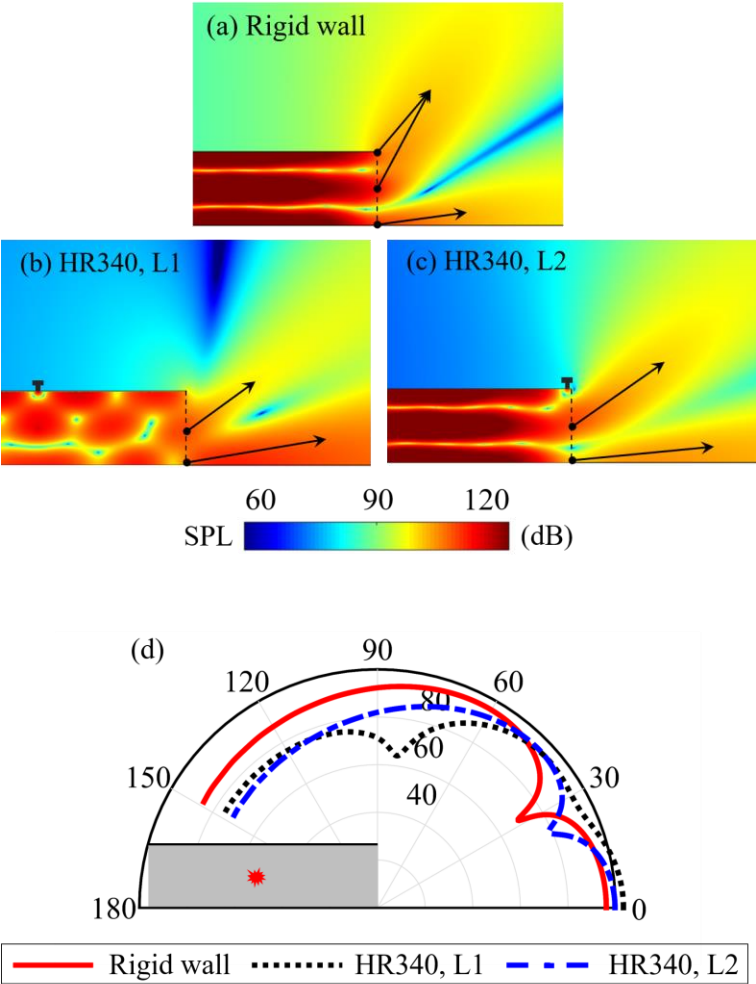
Fig. 5. SPL distributions of the sound fields at 340 Hz: (a) Rigid wall, (b) HR340 at L1, (c) HR340 at L2; and (d) far-field directivity patterns.

To better understand the physics of sound radiation control using an HR, acoustic modal analysis is conducted. Fig. 6 illustrates the absolute modal response coefficients $|G_m|$ for the long enclosure with and without an HR340. In the rigid case, as presented in Fig. 6 (a), the second acoustic mode is dominant. The amplitudes of the second modal responses are significantly reduced when an HR340 is mounted at L1 and L2, as demonstrated in Fig. 6 (b) and Fig. 6 (c), respectively. However, the contributions from the adjacent modes increase as well. Fig. 6 (b) shows that the zeroth and first modes become the main contributors to the total sound pressure field, while Fig. 6 (c) shows that the first four modes contribute to the total sound pressure field.
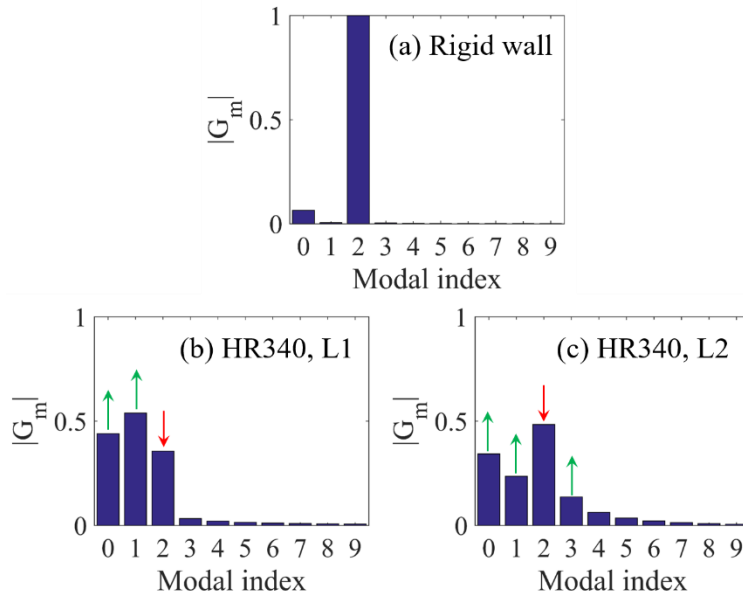
Fig. 6. Absolute modal response coefficients at the opening normalized by the rigid case: (a) Rigid wall, (b) HR340 at L1, and (c) HR340 at L2.

To find the connections between acoustic modes and the SPL distributions of the radiated sound field, the radiation pattern of each single-mode incidence from the enclosure opening is investigated

by the hybrid method [22-24, 36]. The transversal acoustic modal shapes of the rigid long enclosure and the corresponding eigenfrequencies are displayed in Fig. 7 (b). These modes are imposed on the enclosure opening as pressure boundary conditions in COMSOL so that their radiation patterns can be obtained as shown in Fig. 7 (a). Perfectly matched layers (PMLs) are applied to simulate the reflectionless boundaries outside the unbaffled long enclosure.
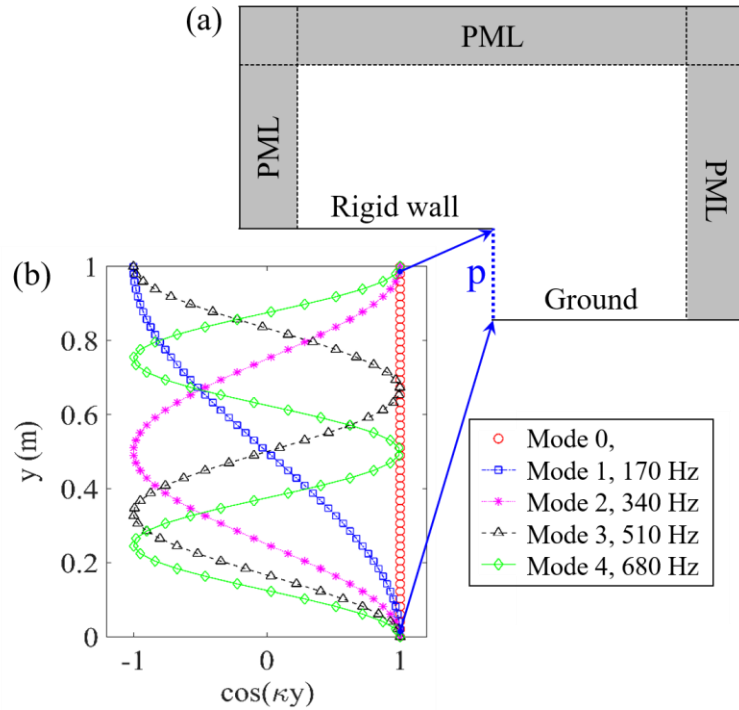

Fig. 7. Schematic diagram of the hybrid method, (a) calculation domain in COMSOL, (b) the transversal modal shapes of the rigid long enclosure and the corresponding eigen-frequencies.

As can be observed in Fig. 8, the radiation patterns of the zeroth to fifth modes at 340 Hz are not symmetric about the centerline of the opening, as demonstrated in Ref. [36]. However, the radiated acoustic modes from the opening tend to propagate upward due to the ground reflection. Besides, the number of radiation lobes at the opening increases with the modal index and is greater than the index by one. Additionally, the higher-order modes dissipate easily, and small lobes merge to form large lobes during the radiation process, as demonstrated from Fig. 8 (d) to Fig. 8 (f). In the far-

field, as presented in Fig. 8 (g), the radiation directivities of the modes differ from each other mainly in front of the opening. After performing the modal decomposition analysis, we find the dominant modal contributors to the radiated sound field. The sound peaks in the shadow zone can then be suppressed by controlling the modal responses of these modes using HRs.
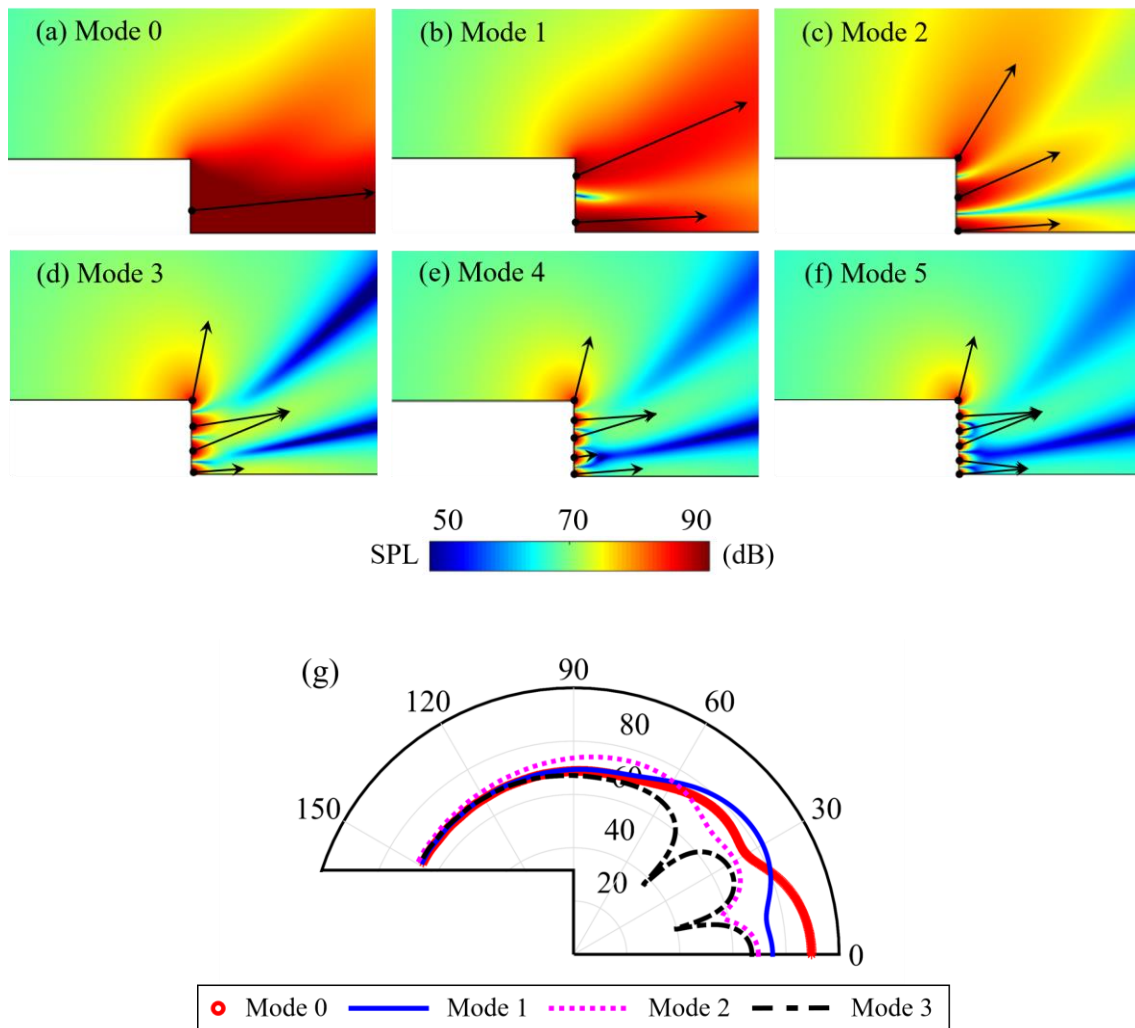

Fig. 8. Radiated SPL fields under single-mode incidence at 340 Hz: (a) Mode 0, (b) Mode 1, (c) Mode 2, (d) Mode 3, (e) Mode 4, (f) Mode 5; and (g) far-field directivity patterns of Mode 0 to Mode 3.

3.3. Diffraction at the enclosure edge

Since only the diffracted sound waves propagate into the shadow zone of the long enclosure, the acoustic properties at the sharp edge, which can be considered as a diffraction point, need to be

further studied. According to the GTD proposed by Keller [37], the diffracted sound pressure field can be calculated by the following equation:

$$p_d = C_d p_i \frac{e^{ikl}}{\sqrt{l}},$$ (51)

where p_d and p_i are the sound pressure at the receiving and diffracting points, respectively, and l is the distance between them. An asymptotically expanded form of the diffraction coefficient is given by

$$C_d = -\frac{e^{i\pi/4}}{2\sqrt{2\pi k}} \left[\sec\left(\frac{\varphi - \phi}{2}\right) + \sec\left(\frac{\varphi + \phi}{2}\right) \right],$$ (52)

where φ and ϕ are the incident and diffraction angles, respectively.
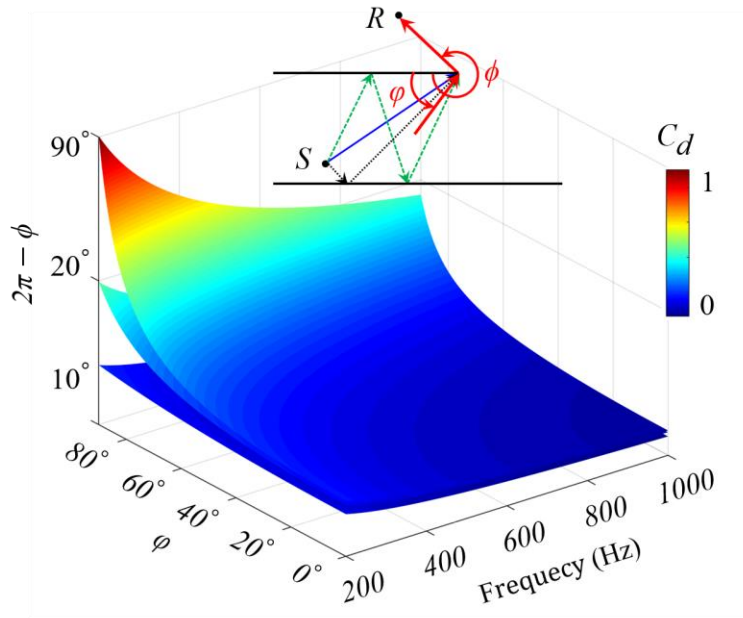
Fig. 9. Change in the diffraction coefficient regarding frequency, incident, and diffraction angles.

The change in the diffraction coefficient regarding the frequency, incident, and diffraction angles is shown in Fig. 9. The diffraction coefficient decreases as the frequency increases. This implies that a sound wave with a long wavelength is diffracted with higher efficiency. In addition, at a specific frequency, the increase in the incident angle obtains a larger diffraction coefficient. This means that the sound wave is

diffracted more effectively if the incident wave impinges normally on the enclosure wall. In contrast, if the incident wave propagates along a parallel direction to the enclosure wall, a minimum diffraction coefficient is observed. Besides, as the diffraction angle increases, it becomes more difficult for sound waves to be diffracted, which results in the uniform decrease of SPL at higher observation angles, as demonstrated in Fig. 5 (d).

Combining Eqs. (50) and (39), the radiated sound pressure field is determined by the pressure and particle velocity response coefficients at the opening. Specifically, they correspond to the amplitude and angle of the incident sound pressure at the edge for the diffraction effect. Their joint effects on the diffraction phenomenon can be represented by a vector quantity, namely, sound intensity. Therefore, attention is then paid to the intensity field around the sharp edge. The sound intensity fields near the enclosure edge with and without HR340 are presented in Fig. 10 using arrow line plots. The length of the line represents the amplitude, and the arrow shows the direction. In the rigid case without an HR, as illustrated in Fig. 10 (a), a ring-shaped sound intensity distribution that rotates counterclockwise is formed near the opening. The incident sound waves reach the sharp edge almost at a perpendicular angle to the wall. The diffraction coefficient, according to the GTD, is close to the maximum. As a result, the far-field SPL at an observation angle of 120 degrees in the shadow zone stands at approximately 88 dB, as presented in Fig. 5 (d). After mounting an HR340 on the wall at L1 and L2, the sound intensities in the shadow zone are reduced, as shown in Fig. 10 (b) and (c), respectively. However, the physics behind these two cases are different. In Fig. 10 (b), an HR340 is mounted exactly above the sound source. The coupling between the HR340 and sound field inside the long enclosure is strong, which distorts the sound distribution near the opening. The sound waves propagate to the diffraction point at a grazing angle to the wall. In this case, based on the GTD, the diffraction coefficient is close to the minimum. In Fig. 10 (c), the HR340 is mounted

near the edge. It produces little effect on the sound field inside the long enclosure. Nevertheless, the sound pressure around the sharp edge is greatly reduced, which also gives rise to the suppression of sound in the shadow zone. Therefore, as demonstrated in Fig. 5 (d), the SPLs at an observation angle of 120 degrees in the shadow zone are 76 dB and 74 dB when an HR340 is mounted at L1 and L2, respectively. The difference between these two cases is that the sound energy propagates mainly along the ground in Fig. 10 (b) and towards the sky in Fig. 10 (c).
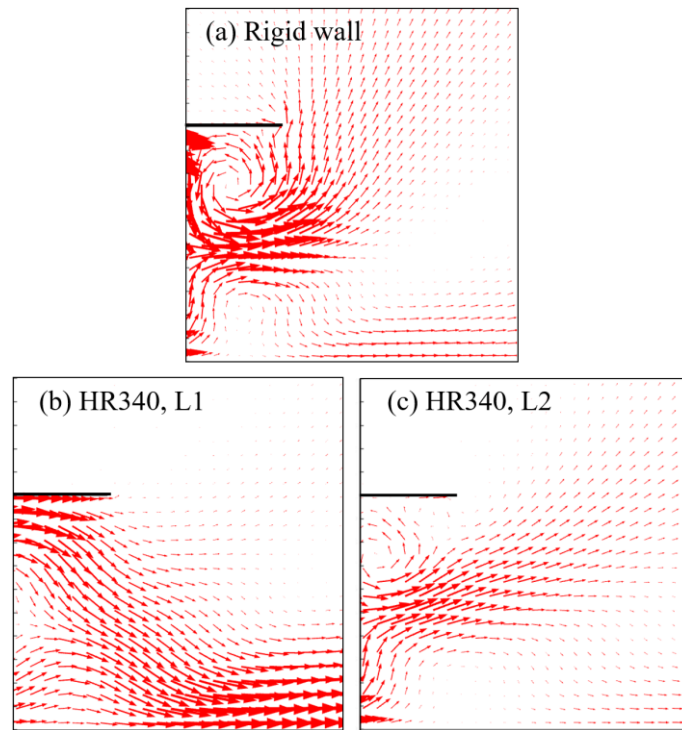
Fig. 10. Sound intensity fields near the sharp edge of the long enclosure at 340 Hz: (a) Rigid case, (b) HR340 at L1, and (c) HR340 at L2.

3.4. Use of multiple HRs

A resonator array consisting of HRs with different natural frequencies can be adopted to reduce the noise level at multiple sound peaks. Therefore, according to the SPL spectra presented in Fig. 4, four HRs, namely, HR340, HR680, HR1020, and HR1360, are designed to suppress the sound peaks

at 340 Hz, 680 Hz, 1020 Hz, and 1360 Hz, respectively. The geometrical configurations of the HRs are presented in Tab. 1. First, the optimized HR locations are obtained based on the maximum mean IL over a frequency bandwidth (20 Hz) centered at the resonant frequencies of HRs. Mathematically, it is expressed as follows:

$$\max\left[IL_{mean}\left(f,x\right)\right]$$

$$IL_{mean}\left(f,x\right)=\frac{\sum_{f-10}^{f+10}\left[SPL_{Rigid}\left(f,x\right)-SPL_{HR}\left(f,x\right)\right]}{N_f} \tag{53}$$

$$\text{subjected to: } x\in\left[-3,0\right]$$

where subscripts 'Rigid' and 'HR' represent the cases without and with the HR, respectively. N_f denotes the total number of sampling frequencies used to calculate the SPL. Fig. 11 indicates the variation of mean ILs at the receiving point R2 (-3, 3) m when different HRs are placed on different locations of the enclosure wall. Small and negative ILs can be observed when the HRs are mounted at the left-hand side of the sound source. This implies that the acoustical coupling between HRs and the long enclosure is weak when they are away from the source. Generally, the optimized locations are between the point source and the sharp edge, and the maximum ILs of HRs decline with increasing frequency. An exception is that two optimal locations are observed for HR680. However, we use (-0.6, 1) m in the following calculations to avoid unfavorable interactions between HRs when the distance between them is too short.

Tab. 1. Geometrical configurations and the optimized locations of HRs in reducing the noise radiated from an unbaffled long enclosure.

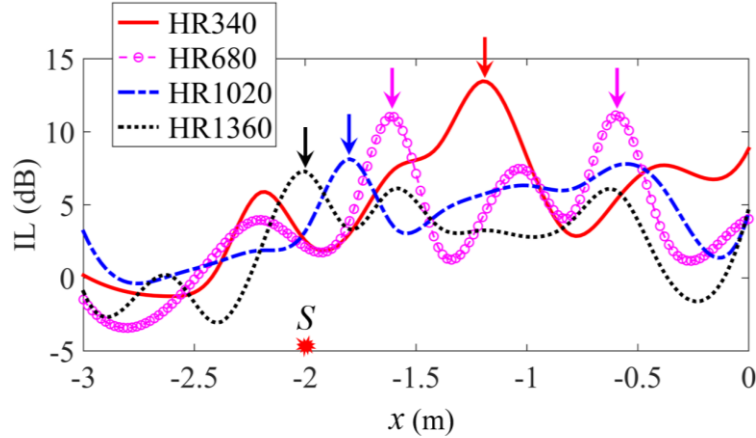| Resonator types	Neck width (m)	Neck length (m)	Cavity width (m)	Cavity length (m)	Optimized Locations (m)
HR340	0.02	0.0381	0.14	0.05	(-1.19, 1)
HR680	0.02	0.02	0.052	0.05	(-1.6,1), (-0.6, 1)
HR1020	0.016	0.02	0.0572	0.02	(-1.8, 1)
HR1360	0.01	0.012	0.028	0.0215	(-2.01, 1)

Fig. 11. Mean IL over the frequency bandwidth of 20 Hz centered at the resonant frequencies of HRs against their locations.

The directivity patterns of the radiated sound field with a single HR and multiple HRs are shown in Fig. 12. Compared with the rigid case without a resonator, the SPLs in the shadow zone are significantly reduced by both a single HR and multiple HRs. Due to the favorable or unfavorable interactions among HRs and the long enclosure, the performance of multiple HRs is superior to a single HR at 340 Hz and 1360 Hz, but inferior to a single HR at 1020 Hz. Overall, multiple HRs can reduce multiple SPL peaks. To examine whether there are undesirable results in this optimized configuration, the ILs of a single HR and multiple HRs are compared in Fig. 13. In general, as presented in Fig. 13 (a), (b), and (d), the performance of multiple HRs can maintain the performance of the corresponding single HR in a certain frequency bandwidth. In Fig. 13 (c), the IL of multiple HRs is smaller than that of a single HR1020, which results from undesirable interactions among HRs and the long enclosure. However, unexpected IL peaks appear in other frequency ranges that result from favorable interactions among HRs and the sound field inside the long enclosure. From the above analysis, a resonator array consisting of HRs with different natural frequencies can be adopted to reduce the noise level at multiple sound peaks provided that their locations are optimized
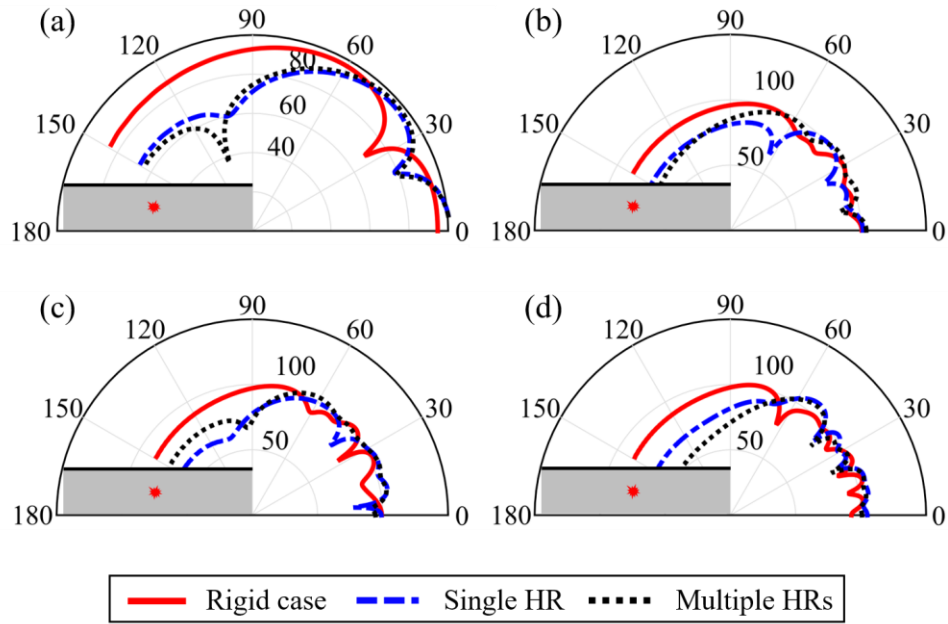
30

in advance.

Fig. 12. Far-field directivity patterns (dB) of the radiated sound field in rigid, single, and multiple HRs

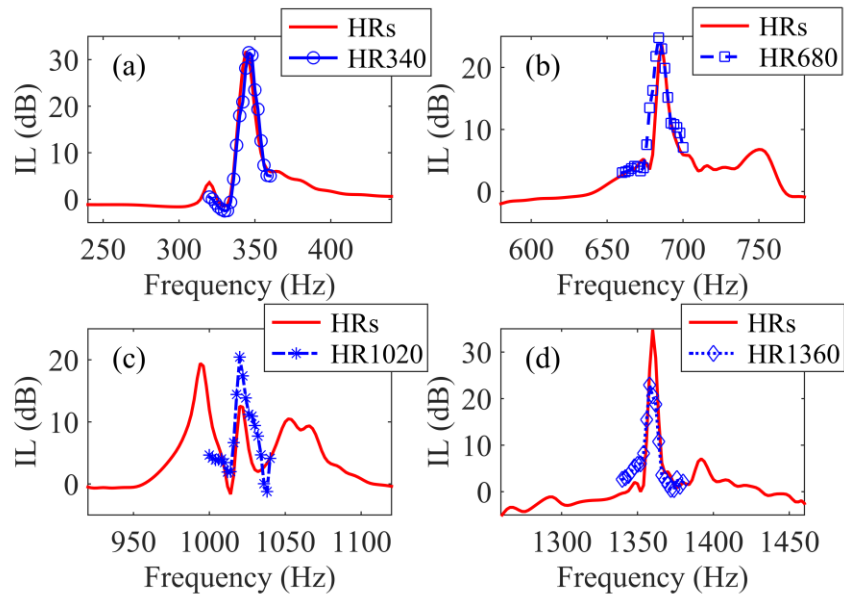conditions at (a) 340 Hz, (b) 680 Hz, (c) 1020 Hz, and (d) 1360 Hz.

Fig. 13. Comparison of ILs between HR array and single HR at R2, (a) HR340, (b) HR680, (c) HR1020,

and (d) HR1360.

3.5. Source effects

In practice, there are various types of noise sources inside an unbaffled long enclosure. Therefore, preliminary investigations are conducted to explore the effects of source on the sound radiation phenomenon. Four cases, namely, (1) plane-wave incidence with amplitude of 1 Pa, (2) single point source Q_1=0.01 m²/s at (-2, 0.5) m, (3) single point source Q_2=0.02 m²/s at (-1, 0.5) m, and (4) two point sources Q_1 and Q_2 at (-2, 0.5) m and (-1, 0.5) m, respectively, are considered here. Directivity patterns of the radiated sound fields at specific frequencies are presented in Fig. 14.
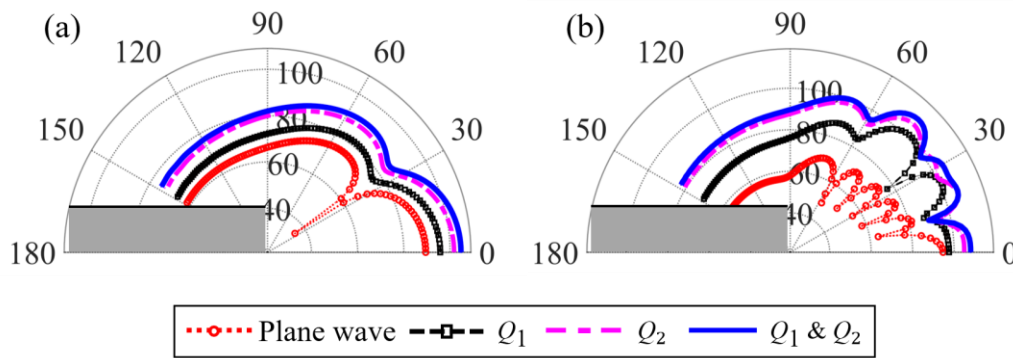

Fig. 14. Directivity patterns of the radiated sound field with different types of sound sources at (a) 300 Hz and (b) 1000 Hz.

As illustrated in Fig. 14 (a), the radiation patterns of the plane-wave and point source cases are similar at 300 Hz. This implies that plane-wave is the dominant mode radiating from the enclosure opening when the frequency of interest is relatively low. However, the size of the lobes in the point source cases becomes large at high frequency compared with the plane-wave case, as presented in Fig. 14 (b). This is the result of the superposition of higher-order modes radiation. In addition, the SPLs are very similar for the case of multiple sources and the source Q_2 case, as the sound field is dominated by the source with a higher volume velocity strength. Besides, the amplitude and location of the point sources also influence the radiated sound field which will be analyzed in future work.

4. Experimental studies

Experimental studies are carried out to validate the theoretical model proposed in Section 2 and verify the feasibility of using HRs to reduce the noise radiated from a long enclosure. The schematic diagram of the test rig is demonstrated in Fig. 15 (a). The experiment is performed in an anechoic chamber with an effective size of 6 m in length, 6 m in width, and 3 m in height. As the theoretical model was established in a 2D configuration, we designed a quasi-2D test rig [38-40], which is presented in Fig. 15 (b). It is constructed by two parallel-arranged acrylic plates of 2.4 m long, 1.2 m wide, and 0.02 m thick. The distance between them is kept at 0.04 m to form a quasi-2D space below approximately 4250 Hz. One side of the test rig is closed using a rigid plate to mimic the ground, and another rigid plate is inserted into the quasi-2D space to simulate the wall. According to the dimensions of the test rig, the distance between the ground and the wall is designed to be 0.2 m, and the far-field observation radius is chosen as 0.6 m. In addition, to simulate the infinite region outside the long enclosure, a layer of wedge-shaped Melamine foam is placed at the side openings to build non-reflection boundaries. The total heights of the wedges are 0.2 m as illustrated in Fig. 15 (b). According to the quarter wavelength rule, they can achieve non-reflection boundaries above about 450 Hz.

The whole test rig is supported by a frame made of aluminum extrusions. Two A0 papers printed with the polar and Cartesian coordinate systems are pasted on the backside of the transparent acrylic plate to locate the measurement points. A Tannoy loudspeaker connected to a long brass pipe of 1 m in length and 25 mm in diameter is applied to simulate a monopole point source. Measurements of the directional characteristics of this source were conducted, and it was observed that the deviations in all directions were within 1 dB for frequencies above 200 Hz [3, 22]. The harmonic sound source is produced by a signal generator, output by an A/D converter (NI 4431), amplified by

a power amplifier (LA 1201), and played by the loudspeaker. Two microphones (B&K 4189) are connected to a conditioning amplifier (B&K NEXUS) and data acquisition module (NI 9234). They move along the observation radius and collect acoustic signals every five degrees of the observation angle. The testing system is controlled by a LabVIEW program, which possesses the merits of good stability and high real-time performance in the targeted frequency range.
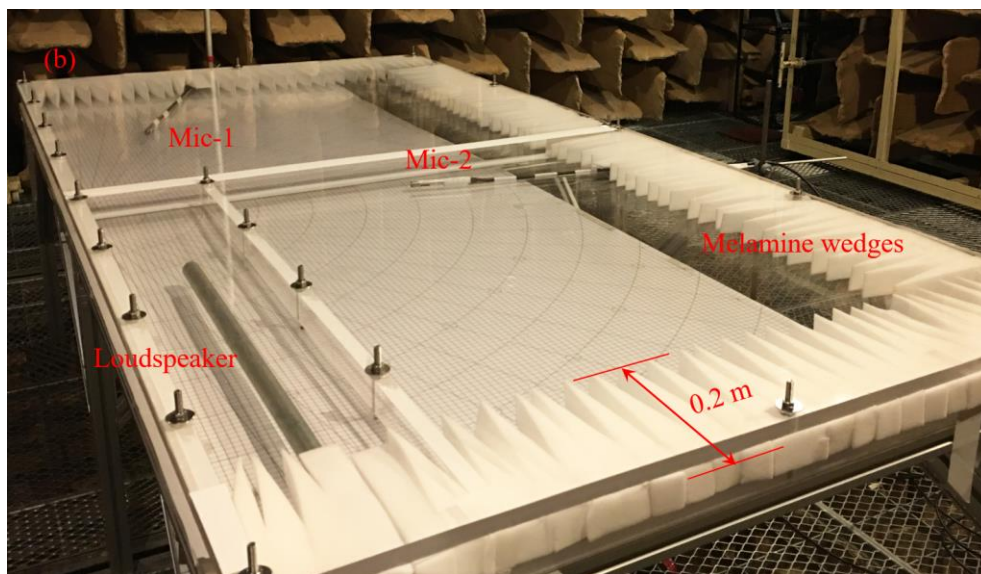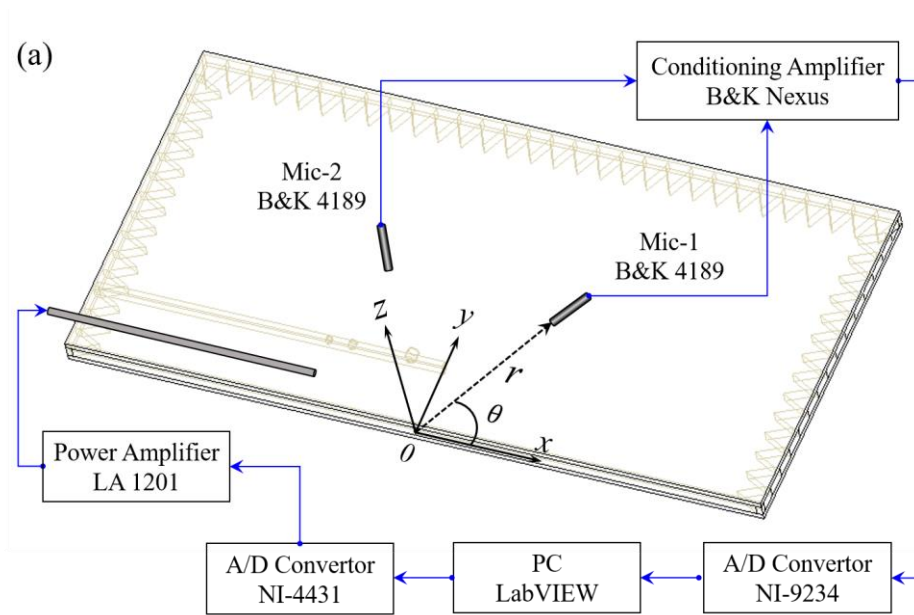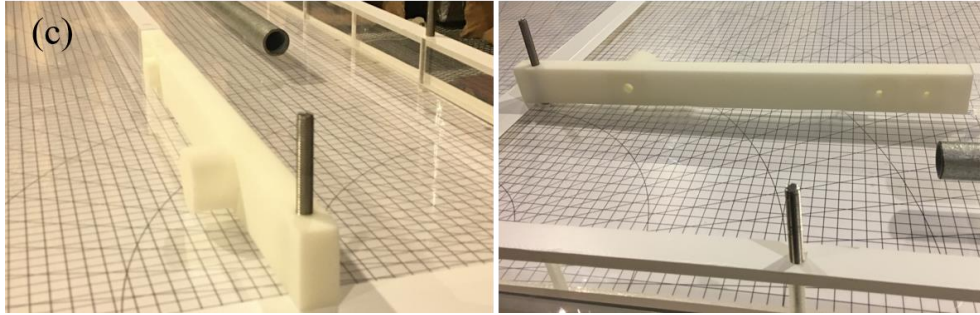
Fig. 15. Experimental setups: (a) the schematic diagram of the quasi-2D test rig, (b) photography of the test rig in an anechoic chamber, (c) Helmholtz resonators on the wall.

Considering the performance of the loudspeaker and the dimensions of the test rig, the location and volume velocity strength of the monopole point source are set as (-0.4, 0.1) m and 0.002 m²/s, respectively, in the experiment. First, the far-field directivity patterns of the radiated SPL field are measured and compared with the theoretical results, as presented in Fig. 16. Good agreement can be observed between the theory and experiment even though there are discrepancies. They are caused by various factors, such as the installation accuracy of the test rig, the quality of the loudspeaker, the performance of the Melamine foam wedges, and the precision of positioning.
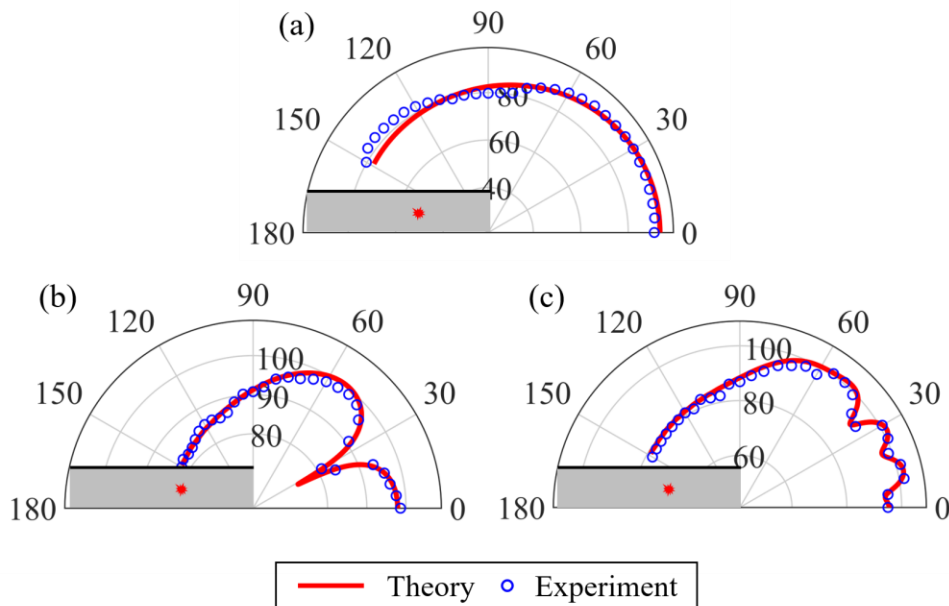
Fig. 16 Directivity patterns of the radiated SPL field obtained by the W-H technique and experiment at

(a) 500 Hz, (b) 2000 Hz, and (c) 4000 Hz.

Then, the feasibility of using HRs to reduce the radiated noise from a long enclosure is verified by the experiment. Considering the height of the long enclosure in the test rig, the first SPL peak appears at 1700 Hz. However, the corresponding HRs are too small to manufacture and install if we adopt a one-fifth scaled-down model of the long enclosure considered in Section 3. Besides, HR340 is too large to be mounted in the quasi-2D space. Therefore, only three cylindrical HRs, HR680, HR1020, and HR1360, fabricated of photosensitive resin using the 3D printing technique, are mounted on the enclosure wall to reduce the radiated noise even though SPL peaks do not appear in the targeted frequency range. The experimental results of the SPL spectra at (-0.6, 0.6) m are presented in Fig. 17. Clear sound reductions can be observed around 680 Hz, 1020 Hz, and 1360 Hz. The average ILs reach 2.1 dB, 8.3 dB, and 11.9 dB within the bandwidth of 20 Hz centered at these frequencies.
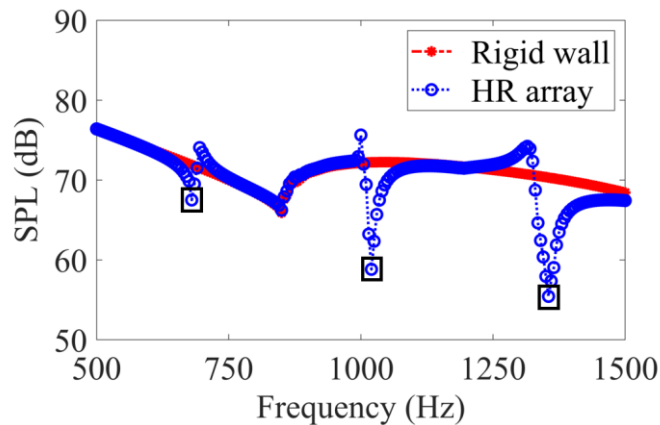

Fig. 17. Experimental results of SPL spectra at (-0.6, 0.6) m with and without HR array.

In addition, measured directivity patterns of the radiated SPL field with and without an HR array at 680 Hz, 1020 Hz, and 1360 Hz are presented in Fig. 18. Clear sound reductions are obtained, especially in the shadow zone. In brief, although the radiated SPL spectrum in the scaled-down test rig is different

from that in Fig. 4 (b), the experimental results demonstrate that using an HR array can reduce the radiated noise in the shadow zone around the targeted frequencies.
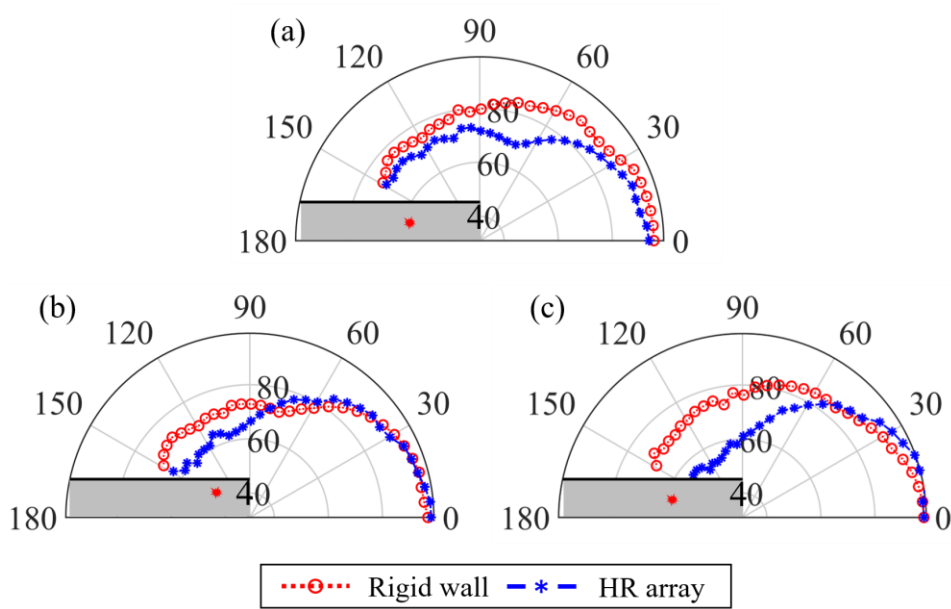

Fig. 18. Measured directivity patterns of the radiated SPL field with and without HR array at (a) 680 Hz, (b) 1020 Hz, and (c) 1360 Hz.

5. Conclusions

The prediction and suppression of the sound inside and outside an unbaffled long enclosure are theoretically, numerically, and experimentally investigated. Formation mechanisms of the radiation directivity patterns are explored. HRs are adopted to attenuate the radiated noise. The following conclusions are made:

1. A theoretical model capable of coupling the interior and exterior acoustical fields of an unbaffled long enclosure with the ground is established. It is proven to be an effective tool for the analysis of sound radiation phenomena and the introduction of appropriate noise control strategies.

2. The sound peaks and directivity patterns are closely related to the acoustic modes and the modal

responses at the opening. With the appropriate design of HRs, the dominant modal responses at the peak frequencies of the SPL spectrum are significantly reduced, which results in the amplitude reduction of the incident sound wave at the top edge of the enclosure. In addition, the direction of the incident wave bends slightly towards the parallel direction along the wall surface. Thus, the diffraction wave that propagates from the top edge to the shadow zone is attenuated.

3. Quasi-2D experiments were conducted to verify the proposed theoretical model and demonstrate the feasibility of using HRs to attenuate radiated noise. Three resonators, HR680, HR1020, and HR1360, were applied to reduce the noise at 680 Hz, 1020 Hz and 1360 Hz, respectively. The average ILs at (-0.6, 0.6) m reach 2.1 dB, 8.3 dB, and 11.9 dB, respectively, within a bandwidth of 20 Hz centered at these frequencies.

Acknowledgements

References

[1] T. Ishizuka, K. Fujiwara, Performance of noise barriers with various edge shapes and acoustical conditions, Appl. Acoust. 65 (2) (2004) 125-141.

[2] K. M. Li, M. P. Kwok, M. K. Law, A ray model for hard parallel noise barriers in high-rise cities, J. Acoust. Soc. Am. 123 (1) (2008) 121-132.

[3] K. M. Li, M. K. Law, M. P. Kwok, Absorbent parallel noise barriers in urban environments, J. Sound Vib. 315 (1-2) (2008) 239-257.

[4] Y. H. Kim, G. G. Song, J. H. Park, S. Y. Kim, S. C. Lee, Acoustic characteristics of tunnel-shaped noise barriers, in: INTER-NOISE and NOISE-CON Congress and Conference Proceedings, 2019.

[5] J. Kang, Reverberation in rectangular long enclosures with geometrically reflecting boundaries, Acta Acust. Acust. 82(3) (1996) 509-516.

[6] J. Kang, Acoustics in long enclosures with multiple sources, J. Acoust. Soc. Am. 99 (2) (1996) 985-989.

[7] W. P. Yang, Z. B. Wang, Y. S. Choy, Prediction of sound radiation from an unbaffled long enclosure with the ground, Mech. Syst. Sig. Process. 149 (2021) 107232.

[8] K. M. Li, K. K. Iu, Propagation of sound in long enclosures. J. Acoust. Soc. Am. 116 (5) (2004) 2759-2770.

[9] P. E. Doak, Excitation, transmission and radiation of sound from source distributions in hard- walled ducts of finite length (i): the effects of duct crosssection geometry and source distribution space-time pattern, J. Sound Vib. 31 (1) (1973) 1–72.

[10] S. Félix, J. B. Doc, M. A. Boucher, Modeling of the multimodal radiation from an open-ended waveguide, J. Acoust. Soc. Am. 143 (6) (2018) 3520-3528.

[11] W. Duan, R. Kirby, A hybrid finite element approach to modeling sound radiation from circular and rectangular ducts, J. Acoust. Soc. Am. 131 (5) (2012) 3638.

[12] A. Seybert, C. Cheng, T. Wu, The solution of coupled interior/exterior acoustic problems using the boundary element method, J. Acoust. Soc. Am. 88 (1990) 1612-1618.

[13] L. H. Huang, G. R. Chen, W. S. Hwang, Sound propagation near tunnel outlets, J. Chin. Inst. Eng. 24 (3) (2001) 321-328.

[14] S. Sakamoto, Road traffic noise prediction model "ASJ RTN-Model 2013": Report of the Research Committee on Road Traffic Noise, Acoust. Sci. Tech. 36 (2) (2015) 49–108.

[15]   G. Gabard, R. J. Astley, Theoretical model for sound radiation from annular jet pipes: far-and near-field solutions, J. Fluid Mech. 549 (2006) 315–341.

[16]   S. Wang, J. Tao, X. Qiu, Performance of a planar virtual sound barrier at the baffled opening of a rectangular cavity, J. Acoust. Soc. Am. 138 (5) (2015) 2836-2847.

[17]   S. Wang, J. Tao, X. Qiu, Controlling sound radiation through an opening with secondary loudspeakers along its boundaries, Sci. Rep. 7 (1) (2017) 1-6.

[18]   S. Wang, J. Tao, X. Qiu, J. Pan, Mechanisms of active control of sound radiation from an opening with boundary installed secondary sources, J. Acoust. Soc. Am. 143 (6) (2018) 3345-3351.

[19]   D. H. Crombie, D. C. Hothersall, The performance of multiple noise barriers. J. Sound Vib. 176 (4) (1994) 459-473.

[20]   A. D. Rawlins, Radiation of sound from an unflanged rigid cylindrical duct with an acoustically absorbing internal surface, Proc. R. Soc. A 361 (1704) (1978) 65-91.

[21]   C. Yang, J. Pan, L. Cheng, A mechanism study of sound wave-trapping barriers, J. Acoust. Soc. Am. 134 (3) (2013) 1960-1969.

[22]   Z. B. Wang, Y. S. Choy, Tunable parallel barriers using Helmholtz resonator, J. Sound Vib. 443 (2019) 109-123.

[23]   Z. B. Wang, Y. S. Choy, Acoustical coupling and radiation control of open cavity using an array of Helmholtz resonators, Mech. Syst. Sig. Process. 130 (2019) 632-648.

[24]   Z. Wang, Y. S. Choy, C. Wang, Vibro-acoustic analysis of parallel barriers integrated with flexible panels, J. Sound Vib. 489 (2020) 115653.

[25]   X. Wang, D. Mao, W. Yu, Z. Jiang, Sound barriers from materials of inhomogeneous impedance, J. Acoust. Soc. Am. 137 (6) (2015) 3190-3197.

[26]   X. Wang, X. Wang, W. Yu, Z. Jiang, D. Mao, A theoretical model of barriers having inhomogeneous impedance surfaces, J. Acoust. Soc. Am. 139 (3) (2016) EL63-EL69.

[27]   Y. Xiao, H. Lai, Q. Li, X. Wang, X. Wang, Improved interference-type sound barriers: Use of hyperbolic phase modulation, Appl. Acoust. 161 (2020) 107186.

[28]   S. H. Seo, Y. H. Kim, Silencer design by using array resonators for low-frequency band noise reduction, J. Acoust. Soc. Am. 118 (4) (2005) 2332-2338.

[29]   C. Cai, C. M. Mak, Acoustic performance of different Helmholtz resonator array configurations, Appl. Acoust. 130 (2018) 204-209.

[30]   D. Li, L. Cheng, G. H. Yu, J. S. Vipperman, Noise control in enclosures: Modeling and experiments with T-shaped acoustic resonators, J. Acoust. Soc. Am. 122 (5) (2007) 2615-2625.

[31]   D. Li, L. Cheng, Acoustically coupled model of an enclosure and a Helmholtz resonator array, J. Sound Vib. 305 (1-2) (2007) 272-288.

[32]   G. Yu, D. Li, L. Cheng, Effect of internal resistance of a Helmholtz resonator on acoustic energy reduction in enclosures, J. Acoust. Soc. Am. 124 (6) (2008) 3534-3543.

[33]   G. Yu, L. Cheng, Location optimization of a long T-shaped acoustic resonator array in noise control of enclosures, J. Sound Vib. 328 (1-2) (2009) 42-56.

[34]   T. A. Khan, M. Ayub, K. Jilani, E-polarized plane wave diffraction by an impedance loaded parallel-plate waveguide located in cold plasma, Phys. Scr. 89 (9) (2014) 095207.

[35]   R. Mittra, S.W. Lee, in: Analytical Techniques in the Theory of Guided Waves, Macmillan, New York, 1971, pp. 91–113.

[36]   Y. H. Tong, Y. W. Kou, J. Pan, Forced acoustical response of a cavity coupled with a semi-infinite space using coupled mode theory, Wave Motion, 73 (2017) 11-23.

[37]   J. B. Keller, Geometrical theory of diffraction, Josa, 52 (2) (1962) 116-130.

[38]   J. Guo, X. Zhang, Y. Fang, R. Fattah, Manipulating reflected acoustic wave via Helmholtz resonators with varying-length extended necks, J. Appl. Phys. 124 (10) (2018) 104902.

[39]   Y. Fang, X. Zhang, J. Zhou, J. Guo, X. Huang, Acoustic metaporous layer with composite structures for perfect and quasi-omnidirectional sound absorption, Compos. Struct. 223 (2019) 110948.

[40]   G. Ji, Y. Fang, J. Zhou, Porous acoustic metamaterials in an inverted wedge shape, Extreme Mech. Lett. (2020) 100648.